Open Archive Toulouse Archive Ouverte (OATAO)

OATAO is an open access repository that collects the work of Toulouse researchers and makes it freely available over the web where possible

This is an author's version published in: **http://oatao.univ-toulouse.fr/23052**

Official URL: https://doi.org/10.1016/j.msea.2014.09.048

Any correspondence concerning this service should be sent to the repository administrator: tech-oatao@listes-diff.inp-toulouse.fr

Study of crack propagation mechanisms during Charpy impact toughness tests on both equiaxed and lamellar microstructures of Ti–6Al–4V titanium alloy

Christophe Buirette [a], Julitte Huez [a,*], Nathalie Gey [b,c], Alain Vassel [d], Eric Andrieu [a]

[a] Institut Carnot CIRIMAT, ENSIACET, 4 allée Emile Monso, 31030 Toulouse, France
[b] Laboratoire d'Etude des Microstructures et de Mécanique des Matériaux (LEM3), UMR CNRS 7239, Université de Lorraine, Île du Saulcy, 57045 METZ Cedex 1, France
[c] DAMAS, Laboratory of Excellence on Design of Alloy Metals for Low-Mass Structures, Université de Lorraine, France
[d] Association Française du Titane, 16 quai Ernest Renaud, BP 70515, 44105 Nantes Cedex 4, France

A B S T R A C T

The impact toughness of two highly textured rolled plates of Ti–6Al–4V alloy with an α equiaxed and an α lamellar microstructures has been investigated.

The results show a strong anisotropy of the fracture energy for both materials and underline that a coincidence of the prismatic planes with the shear bands at the notch tip is favorable for higher fracture energies. Moreover, it is pointed out, as it was already done by previous studies, that the α lamellar microstructure presents higher fracture energy than the α equiaxed one.

Thanks to electron back scattering diffraction, and tensile tests, local microstructure heterogeneities, called macrozones, have been observed and characterized. Their size depends on microstructure element and is larger for α lamellar microstructure than for the α equiaxed. High strain is localized on the macrozones favorably oriented for prismatic slip with respect to the direction of impact and leads to a particular dimple free zone on the fracture surface.

The contribution of these macrozones in the fracture behavior, and more precisely on the crack propagation rate was evaluated; thus the effects of the macroscopic texture and of the microstructure element on the impact toughness are discussed separately.

1. Introduction

The biphasic α–β Ti–6Al–4V titanium alloy is an attractive material for the aeronautic, energy and biomedical industries because it presents a high specific strength as well as a strong resistance to crack propagation and corrosion. However, the anisotropic nature of the hexagonal close packed geometry of the α phase can generate different mechanical properties regarding the crystal orientation towards the testing direction. Many authors have already studied the correlation between the α phase crystallographic orientation and the mechanical properties of the alloy, such as Young's modulus, yield strength and impact and fracture toughness, for both single crystals [1,2] and highly-textured materials [1–7]. In most cases, high values of these properties are related to an orientation of the crystal toward the solicitation axis that allows the activation of the easiest slip system, i.e. prismatic slip, which leads to the accumulation of high plastic strain energy.

The crystallographic texture is not the only parameter to affect mechanical properties. The microstructure of the Ti–6Al–4V alloy, through the size of its microstructural elements like α grains, prior β grains, α platelets, and their width and organization as a colony or in a basketweave formation also play major roles in the mechanical properties. Table 1, which presents results from the literature, shows that for a unique type of microstructure, various impact toughness values were observed depending on the crystallographic texture or morphology and surface fraction of both phases. As a matter of fact, materials should have similar crystallographic textures to enable the comparison of different types of microstructures.

The aim of this paper is to study the Charpy impact toughness of two highly textured rolled plates of Ti–6Al–4V alloy, one with an α equiaxed and one with an α lamellar microstructure. This

investigation will study the mechanical response of the alloy due to both its microstructure and its crystallographic texture.

The first original part of this approach is the sampling, which was performed with similar orientation conditions toward the major α phase crystallographic orientation (knowing the macro-crystallographic texture of both plates). Thus, for a specific specimen crystallographic orientation, the macroscopic results of impact toughness tests and their associated fracture surface observations are analyzed for both materials and correlated only with the microstructure.

The second original part of this research is the proposed worth analysis of the fractured surface in correlation with the submicrostructure and its microtexture that were observed and identified on the plane perpendicular to the fracture plane (thanks to electron back scattering diffraction – EBSD). This analysis allows us to determine the implied deformation mechanisms and the crack propagation modes. These results clearly show that local heterogeneities, called macrozones, strongly impact the crack path and the mechanical behavior of the material. These results add to previous studies made on forged or rolled parts where the presence of macrozones has been identified [8,9].

Finally, to have a complete comprehension of the failure mechanisms involved during impact toughness tests of Ti–6Al–4V and to understand the contribution of the macrozones to the macroscopic results, additional mechanical tests such as bending and tensile tests were performed. Their analysis will constitute the last part of this paper.

2. Materials and procedures

2.1. EBSD characterization

The microtexture and the local texture of the broken Charpy or tensile specimen were characterized by EBSD. We used either the JEOL JSM-6500F scanning electron microscope (SEM) equipped with the Sensitive Channel 5 EBSD System (Oxford Instrument) or the JEOL JSM-6490 SEM equipped with the Fast Acquisition EBSD System (Oxford Instrument). The orientations were measured in a longitudinal cut of the broken specimen after adequate surface polishing. Large orientation maps were acquired in a multi-mapping mode to depict texture variations over millimeter large regions. The beam step was set to 15 μm. Additional EBSD acquisitions with a smaller beam step of 2 μm were run closer to the fracture surface. Inverse Pole Figure maps indicating the Longitudinal Sample Direction in the crystal reference frame (LSD-IPF maps) were acquired. The α local textures were calculated from the large set of orientations by the superposition of Gaussian functions assigned to each measured orientation. The width of each Gaussian function was fixed to 10°. The results were displayed by means of characteristic pole figures (PFs).

2.2. As-received Ti–6Al–4V plates: microstructure and texture

The two Ti–6Al–4V plates were hot rolled to a thickness of 12 mm. Different manufacturing techniques were applied to obtain either an equiaxed or a lamellar α microstructure, each with a sharp α texture. Table 2 indicates the standard chemical composition for Ti–6Al–4V.

The microstructure and the texture of the α equiaxed plate are given in Fig. 1. This plate was obtained by a final deformation and annealing step in the α+β field. In the following, it is referred to as the "α–β annealed" plate. Its microstructure consisted of 80% α equiaxed grains with an average grain size of 30 μm (Fig. 1a and b). The rest was made of aligned α platelets (1 μm thick) separated by thin β layers (in white in Fig. 1b). A strong crystallographic texture

Table 1
Impact toughness values (J/cm²) from the literature for CP–Ti, Ti–4Al–4V and Ti–6Al–4V depending on microstructure (** means no information).

	Lamellar microstructure	Duplex microstructure	Equiaxed microstructure
Ti–6Al–4V [2]	34	**	**
Ti–4Al–4V [2]	92	**	85
Ti–6Al–4V [14]	**	**	28
CP–Ti [15]	**	**	41
Ti–6Al–4V [16]	**	**	41
Ti–6Al–4V [17]	**	36	**
Ti–6Al–4V [18]	49	27	**

Table 2
Standard chemical composition (wt%) of Ti–6Al–4V (Grade 5)

Grade	Al	V	O_{max}	Fe_{max}	C_{max}	N_{max}	Others (each)	Others (max)	Ti
5-Std	5.5–6.75	3.5–4.5	0.20	0.40	0.08	0.008	0.10	0.40	Bal.

was identified by X-ray diffraction; the α phase was mainly oriented with the c-axes parallel to the transverse direction (TD) of the plate, and one prismatic plane was perpendicular to the rolling direction (RD) (Fig. 1c).

The microstructure and the texture of the α lamellar plate are given in Fig. 2. This plate was obtained by a final deformation and annealing step in the β field. In the following, it is referred to as the "β annealed" plate. Its microstructure consisted of α platelets (1 μm thick) aligned to form different colonies of 420 ± 80 μm diameter (Fig. 2a and b) that result from the transformation of prior β grains of around 920 ± 320 μm diameter. A strong crystallographic texture has been identified by a large scale (2 cm²) EBSD analysis (Electron Back Scattering Diffraction); a majority of the c-axes of the α phase were parallel to RD, and one prismatic plane was perpendicular to the normal direction (ND) (Fig. 2c).

Thus, we used two Ti–6Al–4V plates with different microstructures (α equiaxed or lamellar) but with equivalent sharp textures. In fact, by permutation in the transverse and rolling directions, one obtains similar c-axis orientations for both plates. Additional permutation in the rolling and normal directions gives similar prismatic plane orientations.

Further EBSD analysis also revealed the presence of pancake-like macrozones in both Ti–6Al–4V plates. These macrozones correspond to millimeter-size regions elongated in the (RD–TD) plane. Each region exhibits a sharp local texture that is different from one region to the next. This heterogeneous spatial distribution of the α orientations is clearly shown on the EBSD maps acquired in the (TD–ND) and (RD–ND) planes (see Fig. 3 for the "α–β annealed" plate and Fig. 4 for the "β annealed" plate).

Concerning the α–β annealed material, two types of regions with different local textures were found. The first one (in blue in Fig. 3) presents a marked α texture with the c-axes parallel to TD. The other type (in red in Fig. 3) presents a distribution of the c-axes that are spread around the ND and TD.

For the β annealed material, a succession of millimeter-size regions with either sharp or more random local textures was observed throughout the plate thickness. The sharp texture regions consisted of clusters of α colonies with the c-axes parallel to the RD, the main texture component of the plate (in red in Fig. 4). On the contrary, the less textured regions consisted of adjacent α colonies with different orientations.

As H and O are known to affect the mechanical properties of titanium alloys, local chemical analyses were performed using
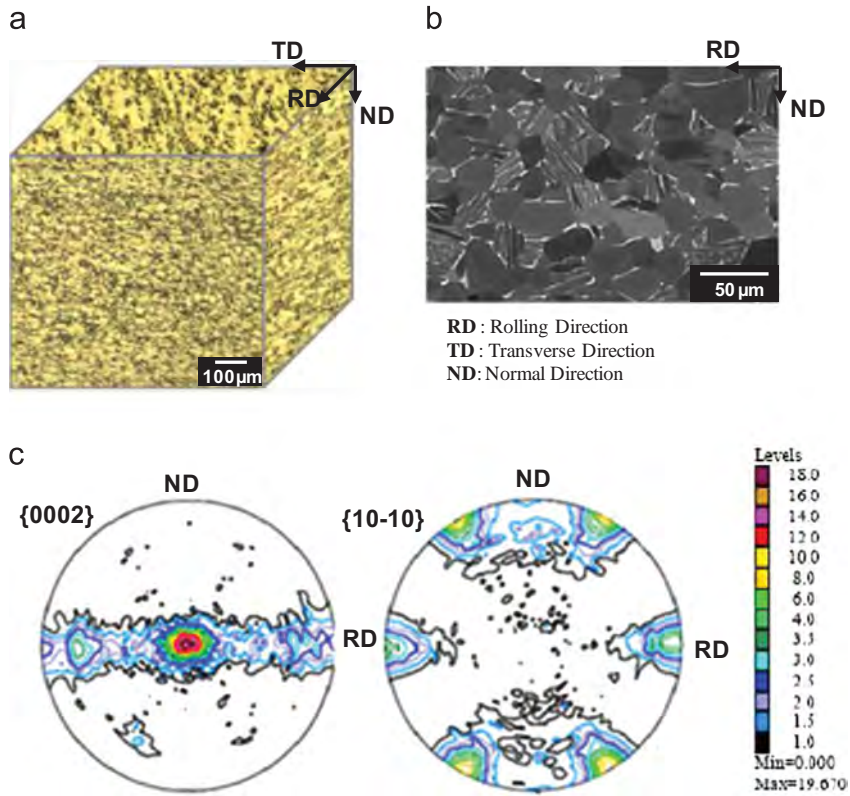
Fig. 1. (a and b) Microstructure of the Ti–6Al–4V α–β annealed material and (c) its associated crystallographic texture.
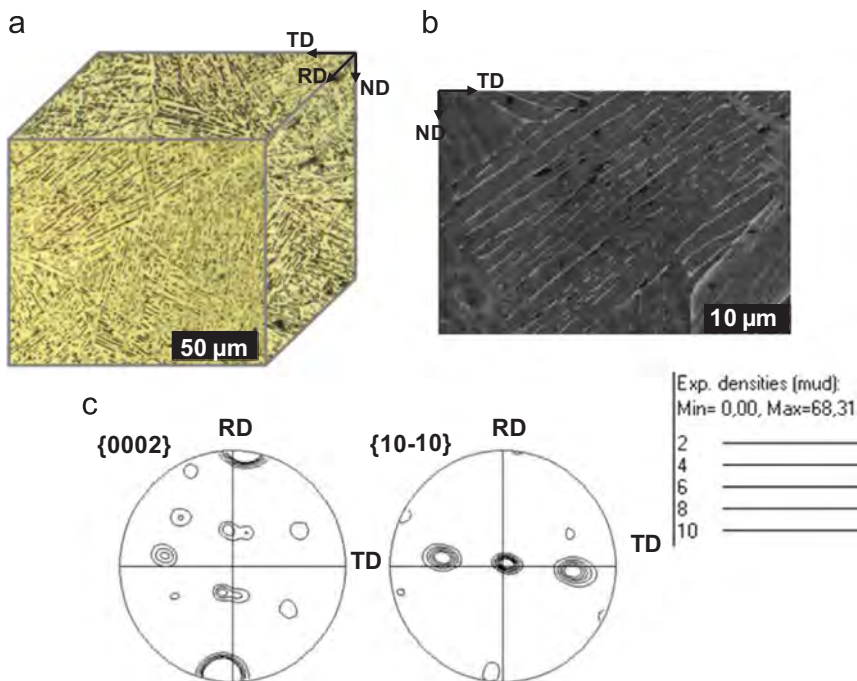

Fig. 2. (a and b) Microstructure of the Ti–6Al–4V β annealed material and (c) its associated crystallographic texture.

Secondary Ion Mass Spectrometry (SIMS) in imaging mode, on TA6V equiaxed microstructure. These analyses allowed us to verify that the local distribution of oxygen and hydrogen was similar inside the macrozone and out of it. So these impurities do not appear to be involved in the following results.

2.3. Mechanical tests

2.3.1. Charpy impact toughness

Impact toughness tests were performed on an Amsler instrument with a capacity of 300 J and an impact speed of 5.23 m/s.
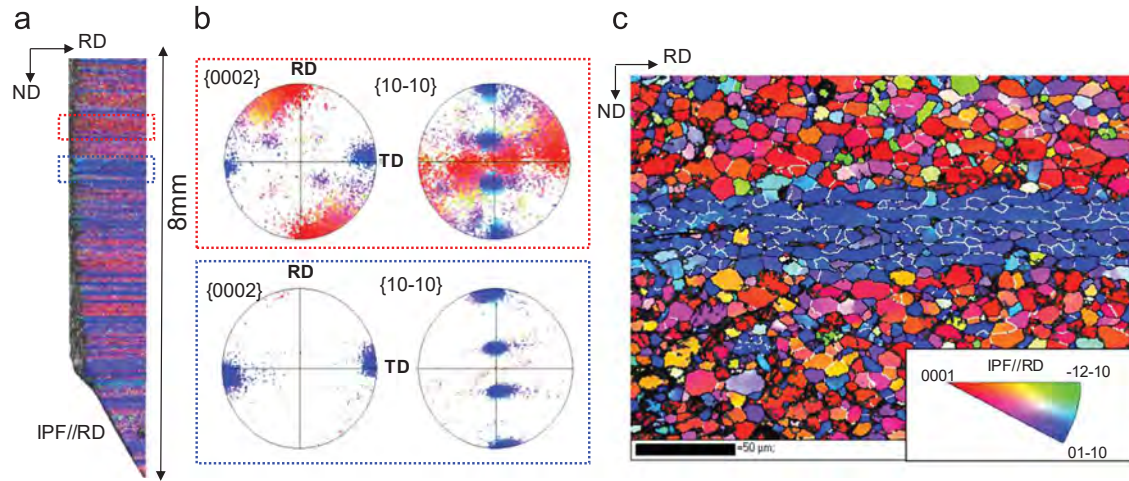
Fig. 3. (a) Large EBSD map through the thickness of the α–β annealed plate reveals the presence of macrozones (in blue and red), (b) pole figures associated with macrozones and (c) high resolution EBSD map. (For interpretation of the references to color in this figure legend, the reader is referred to the web version of this article.)
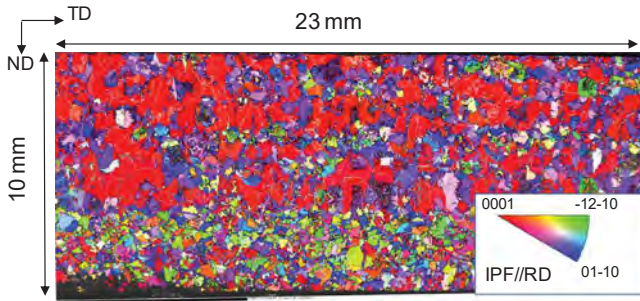

Fig. 4. EBSD map through the thickness of the β annealed plate reveals the presence of macrozones. (For interpretation of the references to color in this figure, the reader is referred to the web version of this article.)
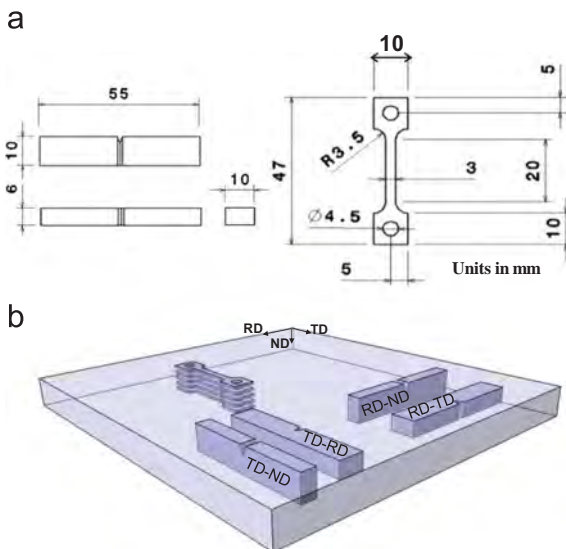

Fig. 5. (a) Geometry of the specimen and (b) schematic of the specimen orientations in the rolled plate.

During the test, when the load increases in the specimen, the plastic deformation localizes to flow along the direction of maximum shear stress, i.e., at an angle of 45° with respect to the loading direction.

A non-standard specimen with lateral notches was used, as it had been shown in a previous study that this type of sample exhibits better reproducibility [10] (Fig. 5a). These notched samples

enable to precisely locate the rupture plane, to limit the propagation of the shear lips and to force the propagation of the crack in planar strain conditions along the width of the notch. From the Charpy impact tests, we distinguish the apparent crack initiation energy (E_i) from the apparent crack propagation energy (E_p) and therefore also the total absorbed energy by $E_t = E_i + E_p$.

For both alloy microstructures, four different plate specimen orientations were tested. Each orientation is designated by four letters (Fig. 5b). With this notation, the first two letters indicate the normal to the notch propagation plane and the last two indicate the crack propagation direction.

This sampling offers equivalent testing conditions regarding the major α orientation for both microstructures. The equivalent configurations are obtained by permutation of RD and TD (for similar c-axis orientation) and RD and ND (for similar prismatic plane orientations).

2.3.2. Tensile tests

Tensile tests were performed on flat specimens piled-up through the plate thickness, and referenced as (TD–ND) with TD the solicitation direction and ND the normal to the specimen's thickness (Fig. 5b). This sampling was chosen to show the effects of macrozones on mechanical properties. An Instron tensile machine was used with a strain rate of $10^{-4}\,\mathrm{s}^{-1}$.

2.3.3. Three point bending tests

Finally, three point bending tests were carried out on TD–ND Charpy specimens (the β annealed plate) in order to simulate low speed impact toughness tests and to observe the different steps involved in the failure of the specimens. An MTS tensile machine was used, and the speed of the indent was set to 0.1 mm/min in order to achieve a strain rate as close to $10^{-4}\,\mathrm{s}^{-1}$ as possible during the test.

3. Results of the Charpy tests

3.1. Anisotropy of the Charpy fracture energies

Results of the Charpy tests are presented in Figs. 6 and 7. Fig. 6 shows the fracture energies; each value is obtained from an average of three tested specimens. Fig. 7 shows the different specimen orientations and corresponding traces of macrozones of the α–β annealed and β annealed samples displayed face to face against their corresponding textures.
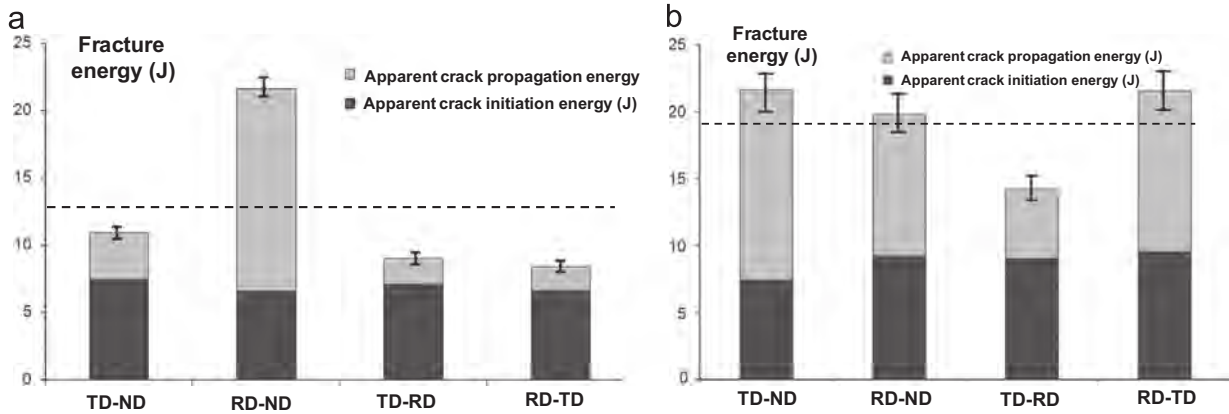
Fig. 6. Fracture energy for different specimen orientations for the (a) α–β annealed (α equiaxed) and (b) β annealed (α lamellar) materials. The dashed black line indicates the mean fracture energy for complete sampling of each studied macrostructure.
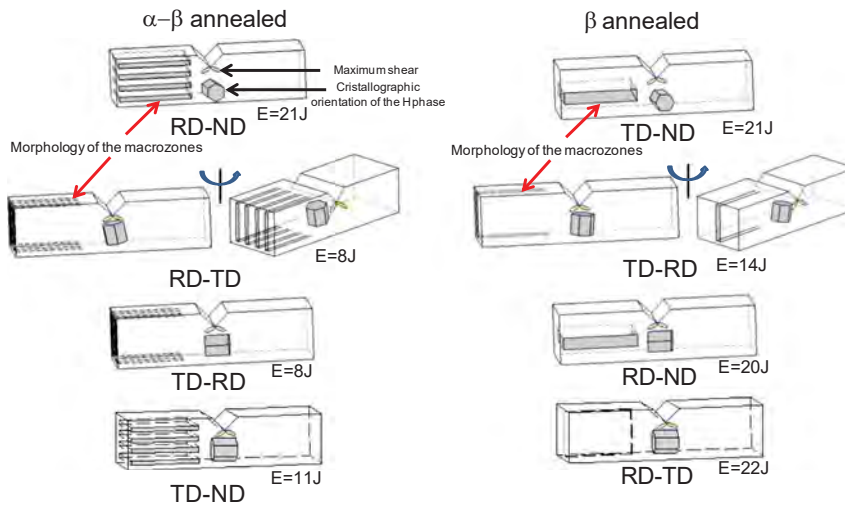

Fig. 7. Schematic of the major α orientation toward the shear bands at the tip of the notch and schematic of the morphology of the macrozones for the α–β annealed and the β annealed materials.

The α lamellar microstructure led to a higher average fracture energy (19 J) than the α equiaxed microstructure (13 J), as expected [19], and it is noticeable that the difference of total absorbed energy between different specimens is explained mainly by a difference in the crack propagation energy [20].

Moreover, a strong anisotropy of the fracture energy was shown for each microstructure. The fracture energy was significantly higher for the RD–ND α equiaxed samples (22 J) compared to the values obtained for the three other specimen orientations (9–11 J). For the α lamellar material, the fracture energy of the TD–RD specimen was quite low (14 J) compared to the fracture energies of other orientations (20–22 J). These observations suggest an important effect of the crystallographic texture on the fracture energies.

Surprisingly, the texture altered the fracture energy differently depending on the type of microstructure and its intrinsic properties. For the α equiaxed microstructure, RD–ND sampling increased the fracture energy (21 J) against the average value (13 J). The equivalent configuration for the α lamellar microstructure TD–ND did not significantly improve the fracture energy (21 J) when compared to the average value (19 J). However, for the α lamellar microstructure, TD–RD samples had smaller fracture energies (14 J) than the average value (19 J). The same was not observed for the α equiaxed microstructure.

3.2. Fractography

Two types of fracture surfaces were observed depending on the sample orientations, regardless of the type of microstructures (Figs. 8 and 9). The fracture surface was either fully covered by dimples, as typically observed for ductile fracture (as observed for TD–ND and TD–RD specimens of the α–β annealed material and for RD–ND and RD–TD specimens of the β annealed material), or covered with dimples and elongated smoothed zones (for RD–ND and RD–TD specimens of the α–β annealed specimen and TD–ND and TD–RD specimens of the β annealed specimen).

When the surface fraction of these smoothed zones increased (e.g., in TD–RD and TD–ND specimens of the β annealed microstructure), the fracture energies also increased (Fig. 10). Thus, these zones may not correspond to a fragile failure or to a quasi-cleavage failure [9–21].

The morphology of these smoothed zones also deserves attention because it was very similar to the morphology of the macrozones. The macrozones were in a pancake shape in the (RD–TD) plane (meaning they were perpendicular to ND) (Figs. 3 and 4). The same was observed for the smoothed zones.

Moreover, for both microstructures, the highest and lowest fracture energy specimens had smoothed zones elongated orthogonal and
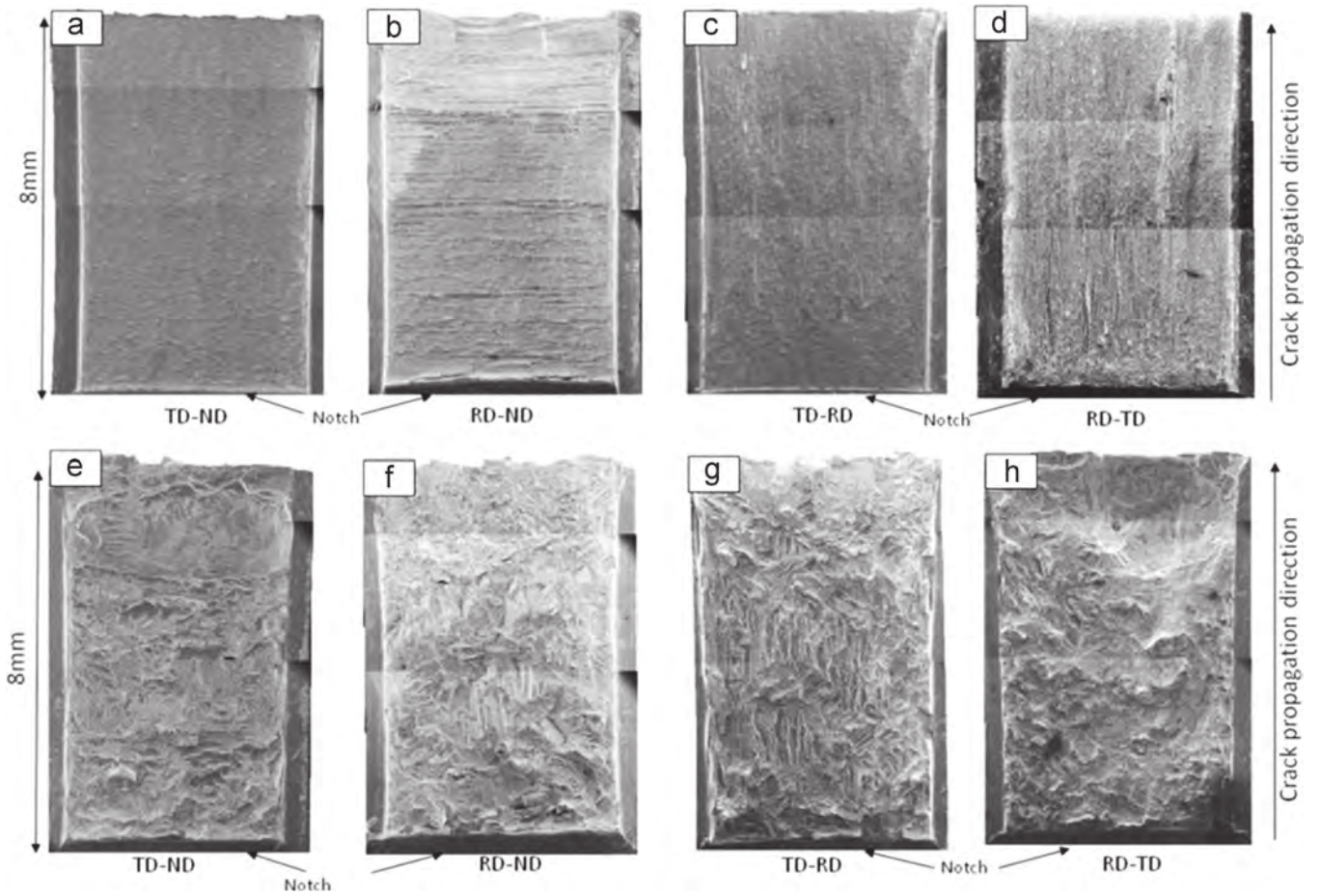
Fig. 8. Representative fracture surfaces for each orientation of the Charpy specimen of the α–β annealed material (a–d) and of the β annealed material (e–h).
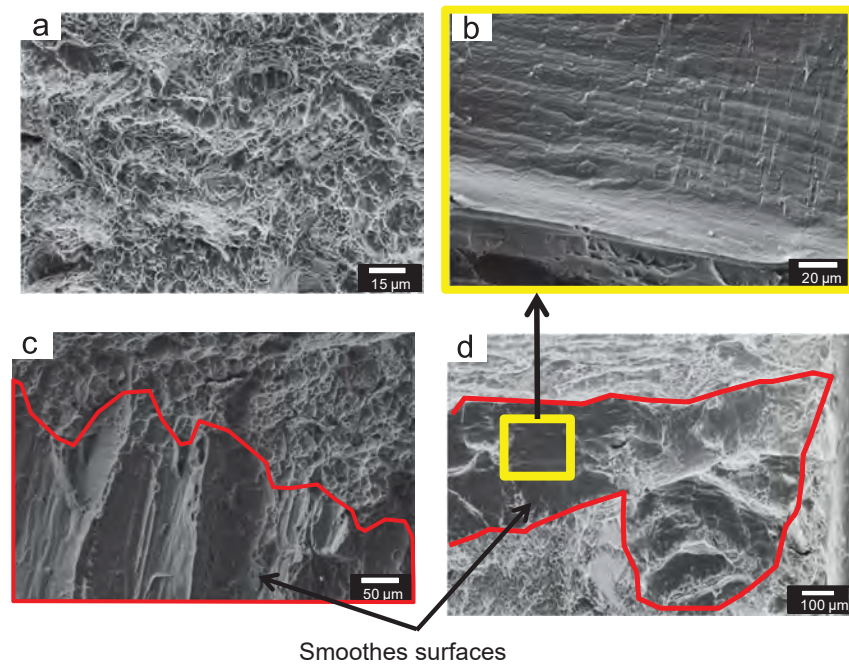

Fig. 9. Fracture surface observations on the α–β and β annealed specimens: (a) ductile failure and (b–d) smoothed zones with very few dimples.

parallel to the crack propagation direction, respectively. This suggests that macrozones play a role in crack propagation for most configurations.

3.3. EBSD analysis close to the fracture surface

Further EBSD investigation demonstrated that the smoothed zones were located within macrozones favorably oriented for prismatic slip under tensile loading. This was shown by EBSD analysis beneath the fracture surface on a perpendicular cut around these smoothed zones. Fig. 11 details the analysis of TD–ND β annealed

specimen. The specimen was cut along the dashed red line to observe the microtexture of the green boxed zone in the (ND–TD) plane (Fig. 11a). This zone corresponded to α platelets arranged in large colonies and oriented with a c-axis parallel to the RD and prismatic plane parallel to the fracture surface, which corresponds to the main texture component of the β annealed plate. The Schmid factor cartography shows that this zone was perfectly oriented for prismatic slip under TD tensile loading (Fig. 11b). Moreover, traces of deformation by crystallographic slip were visible on the polished surface through shearing at the α/β interfaces (Fig. 11c). The slip traces matched with prismatic slip planes, as highlighted in Fig. 11c. Direct SEM observations of the raw smoothed zone at high magnification confirmed the emergence of slip bands (Fig. 11d).
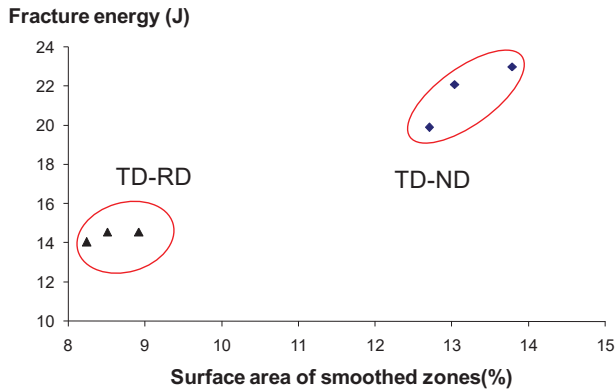
4. Results of the tensile and the three points bending tests

4.1. Macrozone effects on tensile properties

The tensile properties changed significantly as a function of the specimen position along the thickness of the plate, i.e., from one macrozone to the next. Yield stress ($R_{p0.2}$), and maximum stress (R_m) are presented in Fig. 12 for both microstructures according to the sampling detailed in Fig. 5. As an example, for the β annealed plate, specimen No. 2 had a yield stress of only 760 MPa, with a fracture surface composed of both ductile and smoothed zones, whereas specimen No. 4 had a yield stress close to 830 MPa, with a fully ductile fracture (Figs. 12 and 13).
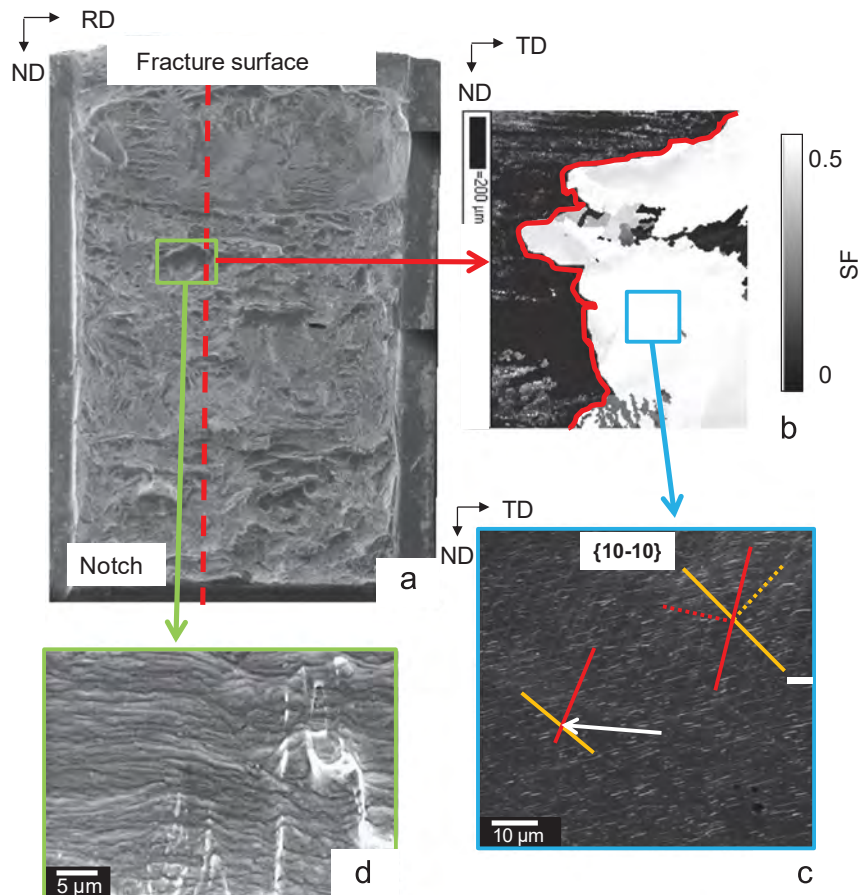
Fig. 10. Relationship between the surface fraction of smoothed zones and the fracture energy of different β annealed specimens.

Fig. 11. (a) Fracture surface of the TD–ND β annealed specimen; (b) Schmid factor map calculated for prismatic slip and tensile direction‖TD. The surface of observation is just under a smoothed zone on the crack path and was obtained by a longitudinal cut of the specimen (dashed red line, same type of cut than the one of the samples exposed in Figs. 3 and 4); (c) SEM picture along the crack path under the selected smoothed zone revealing prismatic slip bands; and (d) direct SEM observation of the selected smoothed zone. (For interpretation of the references to color in this figure legend, the reader is referred to the web version of this article.)
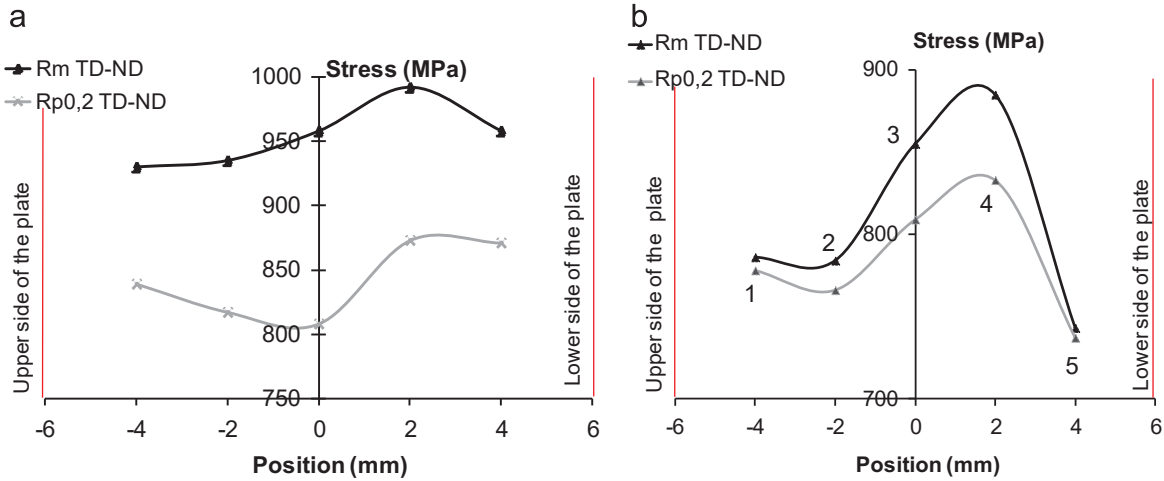
Fig. 12. Heterogeneities of mechanical properties through the thickness of the (a) α–β annealed plates and (b) β annealed plates (position 0 mm corresponds to mid-thickness of the plate); numbers 1–5 correspond to the different samples taken in the plate starting from the upper side.
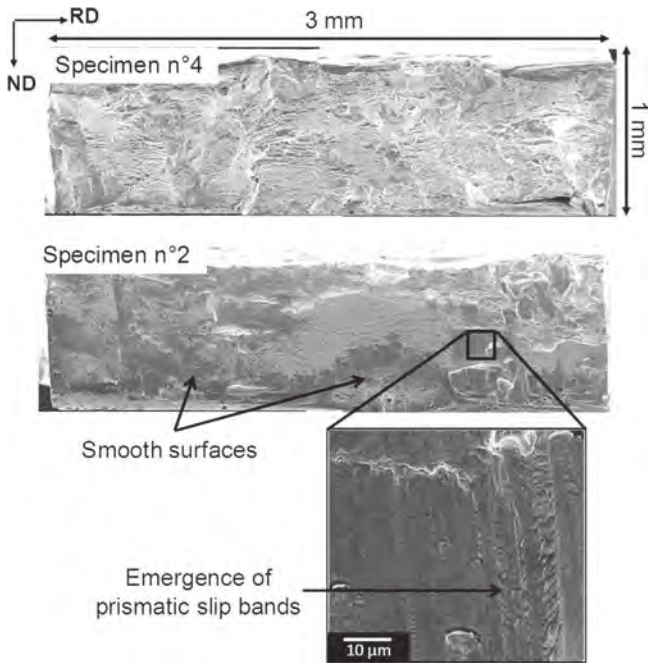

Fig. 13. Fracture surfaces of two specimens taken from the β annealed plate with either a completely ductile surface (No. 4 specimen) or a ductile surface mixed with smooth surfaces (No. 2 specimen).

Further investigations were performed using EBSD to reveal specimen microtexture and to better understand its influence on mechanical behavior. Crystallographic orientation maps were acquired directly on the polished gage length of each specimen (Fig. 14). It can be observed that specimen No. 2, which had a low yield stress, was taken inside a sharp textured region favorably oriented for prismatic slip, whereas specimen No. 4, which had a higher yield stress, was taken out of it. As a consequence, the macrozones are responsible for the low tensile properties and failure occurs due to intense and easy slip over these large zones with similar orientations.

In the literature, it has been reported that different failure modes can occur as a function of triaxiality [22]. Under low triaxiality (< 0.55 for β annealed Ti–6Al–4V [22]), failure without any nucleation or growth of voids has been observed. In the present study, the macrozone in specimen No. 2 behaves as a monocrystal, which has triaxiality close to 0.3 during uniaxial

tensile tests and thus generates a fracture surface without any dimples. As the macrozone is favorably oriented for prismatic slip (Fig. 14b), the No. 2 specimen exhibits a low yield stress. Furthermore, this macrozone is subjected to high plastic strain, which is confirmed by the observations of the emergence of prismatic slip bands on the dimple-free fracture surface (Fig. 13).

To conclude, these tensile tests confirmed the first observations from the Charpy specimens: high strain is localized on the macrozones favorably oriented for prismatic slip and leads to a dimple-free zone on the fracture surface.

4.2. Impact of macrozones on crack propagation behavior through low speed Charpy tests

Additional low speed Charpy tests demonstrated the dual effect of macrozones:

(1) when favorably oriented for slip, high strain localization favors high fracture energies and thus slows down crack propagation and
(2) this accumulation of slip bands results in a low resistance to crack propagation.

Thus, macrozone alignment with respect to the crack propagation path may influence the speed at which the crack propagates.

The fracture surface of TD–ND β annealed specimen broken during this test and its associated curve are presented in Fig. 15. From this curve, two different crack propagation behaviors could be identified: first, when there is a drop in load (steps 1, 3, and 5), a fracture in part of the sample is occurring and thus the crack is propagating at a high speed; second, when the load is constant (steps 2, 4, and 6), plastic deformation of the material is occurring and the crack is propagating slowly or is stopped.

On the fracture surfaces, regions with a high surface fraction of smooth surfaces (regions 2 and 4) could be distinguished from regions where this surface fraction is much lower (regions 1, 3 and 5). This observation, in conjunction with the load–displacement profile, leads to several conclusions regarding crack progression. First, step 1 of the curve corresponds to the initiation of the crack and the propagation inside region 1 of the specimen. During step 2, the crack is slowing down because of the localization of high plastic strain in the macrozones in region 2 (Fig. 16). Once failure has begun in the macrozone, it appears that the crack propagates quickly (step 3) through region 2 and part of region 3. Step 4 corresponds to the end of failure of region 3 and to the strain
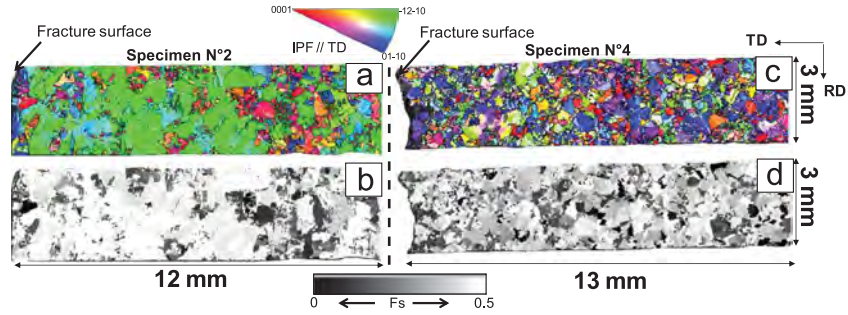
Fig. 14. EBSD crystallographic orientation maps (IPF‖TD) of the gage length of No. 2 (a) and No. 4 (c) specimens of the β annealed plate. Schmid factor map for prismatic slip of the gage length of No. 2 (b) and No. 4 (d) specimens
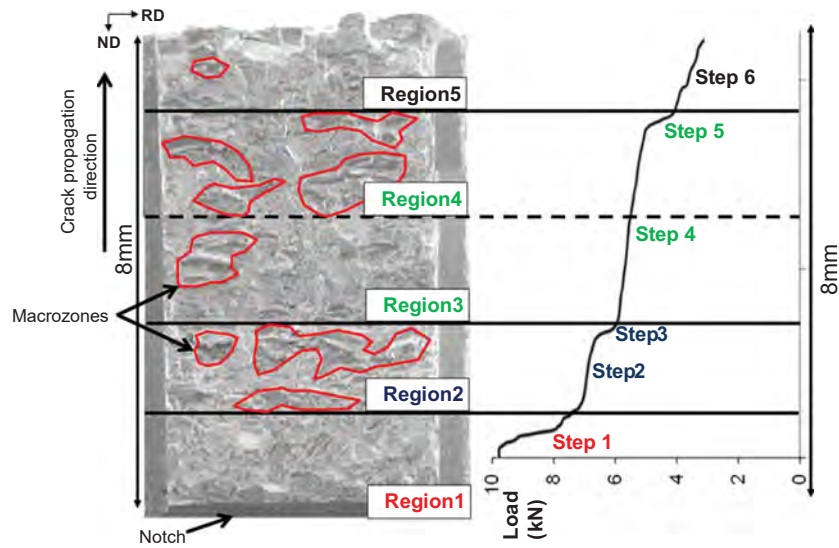

Fig. 15. (a) Fracture surface of a Charpy specimen broken during the bending test and (b) its corresponding load–displacement curve (β annealed material).
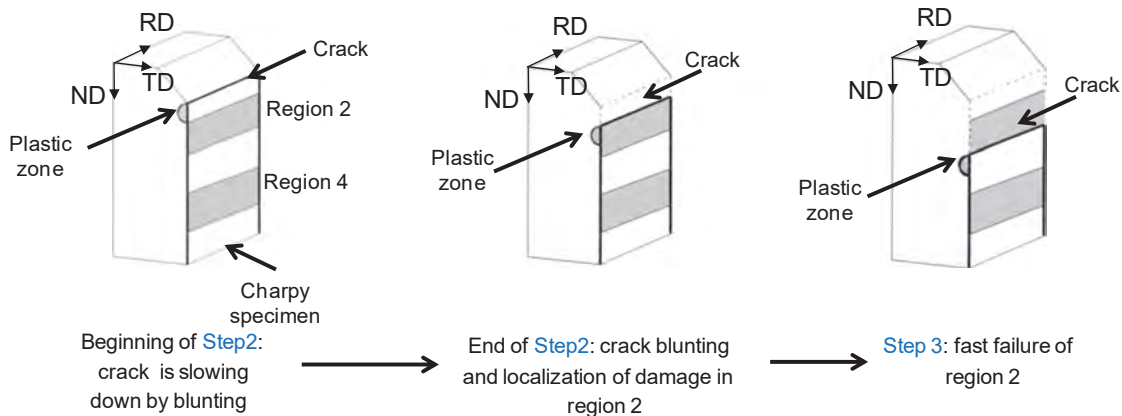

Fig. 16. Schematic of the propagation of the crack through a region with macrozones (gray regions represent those with macrozones).

localization in region 4, containing a high density of macrozones. A high crack propagation rate (step 5) is recorded during the failure of region 4. Finally, the last step corresponds to final rupture in region 5 of the specimen.

To summarize, the macrozone can act either as reinforcement or as a weak point of the material. When favorably oriented for prismatic slip, a particular failure mechanism is involved: high strain localization is observed and promotes high fracture energies. Nevertheless, only low energy dissipation is possible during fast crack propagation inside the macrozone, which counterbalance the benefit of the high strain localization (Fig. 16).

5. Discussion

5.1. Influence of the microstructure on the impact energy

Fig. 6 shows that the mean fracture energy of the β annealed microstructure (19 J) is higher than that of the α–β annealed material (13 J). This result was obtained by averaging the fracture energies for different specimen orientations (but β annealed/α–β annealed orientation equivalent – Fig. 7). Therefore it highlights the unique effect of microstructure on the mechanical properties, regardless of texture effects. As the texture strongly influences the

mechanical properties, it is often difficult to compare the intrinsic effect of the microstructure from the literature (Table 1).

The difference in fracture energy induced by the microstructure is mainly due to the size of microstructural elements that cause bifurcation and thus influences the crack propagation path. Longitudinal cuts were performed on broken specimens, and microstructures were revealed under the crack propagation path by polishing and etching. The comparison of microstructures in Fig. 17 reveals that the crack propagation path is much longer in the case of the β annealed material than in the α–β material (around 11.5 ± 1 mm and 8 ± 1 mm, respectively, which were estimated by image analysis). No secondary crack or crack branching was observed.

As the plastic zone size at the tip of the crack is approximately the same (around 500 µm) for both microstructures, the difference in crack path length between materials is mainly due to the number of α/β interfaces and to the size of microstructural elements that can act as obstacles or bifurcation sites to crack propagation (Fig. 18). For the α–β annealed material, the propagation of the crack is intragranular. As the grain size is small (diameter of 30 µm), a low roughness and a short crack path length will be generated. On the contrary, for the β annealed material, the crack propagates either at the prior β grain boundary, at the interface between two colonies or between two α platelets. Because of the geometry of the platelets (low thickness of 1 µm and long length of 100 µm), the crack easily deviates and creates a long crack path [23].

These explanations of the microstructure influence on impact energy are also consistent with tensile test results (Table 3). Tensile tests show that the fracture energy of the α–β annealed material is three times the energy required to break the β annealed material. Therefore, the difference in impact fracture resistance between the two microstructures is likely due to the crack path tortuosity described above.

5.2. Influence of the global crystallographic texture on the fracture energy

In addition to the microstructure, the crystallographic texture also has a significant impact on the Charpy impact toughness (Fig. 6).

A significant increase of fracture energy is obtained for the (RD–ND) α–β annealed specimen (21 J) against the average value (13 J). For the equivalent β annealed sample orientation (TD–ND specimens), the fracture energy also increases but to a lesser extent compared to the average value (21 J for TD–ND and 19 J for the average value). In fact in these two configurations, the imposed in-plane strain condition at the crack tip can be accommodated by easy crystallographic slip. The c-axis is in the direction of zero strain and any displacement around the crack tip can be achieved by $\langle a \rangle$ slip on prismatic planes. This is highlighted in Fig. 7 where the main α hcp crystal orientation can be compared to the maximum shear bands at the notch tip for the different specimen orientations. Moreover microstructural investigations on the β annealed specimen illustrated in Fig. 11 clearly confirmed intense prismatic slip, especially in the smoothed zone of the fracture surface. Surprisingly, tensile twins ($85° < 11\overline{2}0 >$) were also observed within large α colonies. Similarly the EBSD analysis on the α/β annealed material showed pronounced deformation marks (internal grain misorientation and twins). These additional results are detailed in Ref. [24].

This confirms that the highest fracture energies are obtained when the available crystallographic deformation modes can accommodate the imposed in-plane strain deformation at the crack tip. Such configuration gives the lowest stress at the crack tip and a stable crack propagation. This conclusion is consistent with the works of Tchorzewski et al. [5] and Bowen [6,7]. Interestingly, our study highlights that this favorable texture effect is much more pronounced for the α–β annealed specimen than for the β annealed specimen. In fact, the major microstructure effect

Table 3
Tensile tests results for α–β and β annealed materials. Tensile direction‖ to major c axis; thus, tensile direction is RD for β annealed material and TD for α–β annealed one.

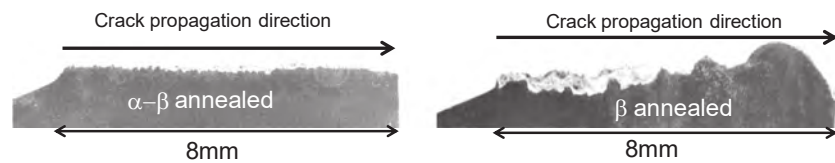| Material	$R_p0.2$ (MPa)	R_m (MPa)	Ar (%)
α–β Annealed	**942** ± 12	**1015** ± 16	**14.5** ± 5.1
β Annealed	**815** ± 12	**846** ± 14	**5.9** ± 1.7

Fig. 17. Crack propagation path on representative broken Charpy specimens of the α–β annealed and β annealed materials.
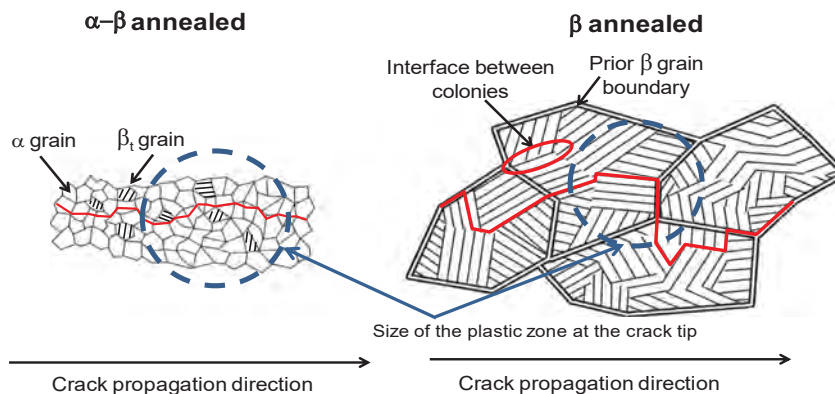

Fig. 18. Schematic of the role of microstructure on the crack propagation behavior for both materials (crack path in red). (For interpretation of the references to color in this figure legend, the reader is referred to the web version of this article.)

of the β annealed specimen leads to high fracture energies whatever the texture (see Section 5.1).

On the contrary, the lowest fracture energies are obtained when the crystallographic deformation modes do not coincide with the shear bands at the crack tip as observed for the RD–TD (α–β annealed) and TD–RD (β annealed) specimens (Fig. 7). It is clear that for this configuration, the deformation modes cannot satisfy the in-plane strain conditions imposed at the notch type. As a consequence, high elastic stress levels arise, favoring voids nucleation and instable crack growth. This was confirmed by the microtexture analysis performed close to the fracture surface for the β annealed specimens (in a similar way as in Fig. 11). Most of the smoothed regions corresponded to large α colonies with the main specimen orientation. Only a few trace of slip bands was observed. However, in the dimpled regions, intense twinning was evidenced (with typical misorientation of $85° < 1\bar{2}10 >$ and $39° < 01\bar{1}0 >$). These plastic deformation modes combine in-plane and through thickness deformation, favoring voids nucleation and instable crack growth.

For the two remaining configurations, the *c*-axis orientation is perpendicular to the crack propagation direction. One can notice that the α phase is not even favorably oriented for prismatic slip under tensile stress in the longitudinal specimen direction. One would expect a low fracture energy. The α–β annealed ones demonstrate indeed low fracture energy. However, those β annealed keep high fracture energy.

In the literature, these two configurations are often considered as intermediate between the worst and the best. Bowen [7,8] pointed out that $\{11\bar{2}1\} < 11\bar{2}6 >$ twinning fulfill the in-plane strain condition for the (TD–ND) α–β annealed and (RD–TD) β annealed configurations. The literature review in Ref. [5] pointed out that these configurations may show high or low toughness. The authors assume that this could be linked to the influence of aligned microstructure (similar to the macrozones highlighted in the present work). However, this influence has never been deeply analyzed.

5.3. Effect of the macrozones on crack propagation behavior during Charpy tests

The bending test results obtained on TD–ND β annealed sample (Section 4.2) have pointed out a dual effect of macrozones. They can act either as reinforcement or as a weak point of the material. When favorably oriented for crystallographic slip, high strain localization is observed and high fracture energies are promoted. However, when the macrozone is large in the direction of the crack propagation, once a crack has nucleated, it propagates fast. As a consequence, only low energy dissipation is possible during fast crack propagation inside the macrozone.

The fracture surfaces of the Charpy specimens suggest that the macrozones could also be involved in the Charpy results (Fig. 8). Indeed, the fracture surfaces highlight the presence of the macrozones through the smoothed zones. From one fracture surface to the other, their density varies, as well as their thickness and alignment against the direction of crack propagation. The implication of the macrozones on the crack propagation mechanisms probably depends on their configurations in the specimen.

The influence of the macrozone thickness (and density) could be catch comparing the RD–ND α–β annealed material (the macrozone thickness is very thin ($\sim 100\ \mu m$) – Fig. 8b) and the TD–ND β annealed material ($\sim 1\ mm$ – Fig. 8e) (alignment and orientation are equivalent). The large macrozones with high strain localization will have less resistance for crack propagation. The β annealed specimens could thus have reduced toughness than expected without macrozones. This could also explain why, comparing these two specimens where the global texture is

favorable to high toughness, the β fracture energy gap from the average value is not so important as the one observed for the α–β annealed one (respectively a gap of 2 J and of 8 J).

Differences in macrozone alignment against the crack propagation direction can clearly be seen on the fracture surfaces of RD–ND and RD–TD α–β annealed specimens (Fig. 8b and d). The α–β annealed material could be considered as a composite material with a stacking of soft and less soft layers (see Fig. 3). When the macrozones (soft layers) are oriented perpendicular to the crack propagation direction (Fig. 8b – RD–ND α–β annealed specimens), the crack propagates through all the layers of the material. As a result, high plastic strain localization and crack blunting occur inside the macrozones. Meanwhile, the relatively low thickness of those macrozones ($100\ \mu m$) and their alternation hinders fast crack propagation rates. So the global texture and the macrozone alignment favor high fracture energy. On the contrary, for the RD–TD specimens the macrozones are oriented parallel to the crack propagation direction. As discussed in Section 5.2, in this configuration, the plastic deformation modes combines in-plane and through thickness deformation, favoring voids nucleation and instable crack growth. The alignment of the macrozones in the crack propagation direction would then favor fast crack propagation. In that case, global texture and macrozone alignment are both not favorable for high fracture energy.

6. Conclusions

Charpy impact tests were carried out on two different microstructures of ring rolling Ti–6Al–4V alloys. Results of fracture energy have been discussed from two well characterized parameters of each material: the microstructure and the crystallographic texture. The EBSD analysis and an original correlation between some fracture surface elements and their nature and crystallographic orientation have been helpful for this characterization.

Then, a specific sampling was chosen in order to isolate the unique effect of the microstructure on the fracture energy. So these conclusions are related to an effect of the macroscopic texture on the impact toughness of first order and an effect of the microstructure of second order.

6.1. Major effect of the global texture on the impact toughness

For each studied microstructure, a strong anisotropy of the fracture energy has been evidenced. The intense crystallographic texture for both microstructures appears to have an influence on the mechanical behavior at a macroscopic and a microscopic scale.

On one hand, plastic strain and energy dissipation will depend mainly on the orientations of the α phase towards the main solicitation direction as well as the orientation of prismatic plane towards shear bands at the notch tip of the specimen. A coincidence of the prismatic planes with the shear bands at the notch tip is favorable for elevated fracture energy whatever the microstructure (illustration with TD–ND β annealed and RD–ND α–β annealed specimens).

6.2. Influence of microtexture elements on fracture behavior

The presence of macrozones in both materials strongly modifies the mechanical response. The macrozone consists of a cluster of α phase with a unique crystallographic orientation. The size of the macrozone is directly correlated to the size of the microstructure which implies α phase in the alloy: α grain size for α–β annealed material, α colony size for β annealed material. When the α phase in the macrozones is favorably oriented for prismatic slip, regarding the solicitation direction a particular failure

mechanism is observed. This one is explained by a low local triaxiality inside the macrozone leading to high strain localization and failure without nucleation or growth of dimples.

Concerning the β annealed material, a fast crack propagation rate has been recorded in the macrozone, which concurrence the high energy dissipation achieved by strain localization. Because of the large scale of the macrozones in the β annealed material, the contribution of the fast crack propagation rate on the fracture energy is more detrimental in this material compared to the one in the α–β annealed.

For the α–β annealed material, the low thickness of the macrozones will then enhance the strain localization effect.

6.3. Unique effect of the microstructure on the impact toughness

When macrozones are not favorably oriented for prismatic slip regarding the solicitation direction, their contribution in the fracture behavior becomes negligible in front of the contribution of the microstructure. This is clearly evidenced on specimens that do not present any smooth surfaces, but have a similar macro-texture: on one hand, RD–TD α–β annealed and TD–ND β annealed specimens, on the other hand, TD–RD α–β annealed and RD–ND β annealed specimens. This is the reason why it was possible to isolate the unique effect of the microstructure (equiaxed or lamellar) on the fracture energy.

In fact, because of coarse microstructural elements and numerous α/β interfaces, the crack path length in the β annealed material is longer than the one in the α–β annealed material. As a consequence, a higher volume of material is submitted to plastic deformation in the β annealed material which also leads to high energy dissipation.

References

[1] E.S. Fisher, C.J. Renken, Phys. Rev. A 135 (1964) 482–494.
[2] A. Zarkades, F. Larson, MCIC Report, Army Materials & Mechanics Research Center, Watertown, Massachusetts 02172, June 1972.
[3] F. Larson, A. Zarkades, MCIC Report, Army Materials & Mechanics Research Center, Watertown, Massachusetts 02172, June 1974.
[4] F. Bridier, P. Villechaise, J. Mendez, Acta Mater. 53 (2005) 355–357.
[5] R.M. Tchorzewski, W.B. Hutchinson, Metall. Trans. A 9A (1978) 113–1124.
[6] A.W. Bowen, Acta Metall. 26 (1978) 1423–1433.
[7] A.W. Bowen, Acta Metall. 23 (1975) 1401–1409.
[8] L. Germain, N. Gey, M. Humbert, P. Vo, M. Jahazi, P. Bocher, Acta Mater. 56 (2008) 4298–4308.
[9] M.R. Bache, Int. J. Fatigue 25 (2003) 1079–1087.
[10] C. Buirette, J. Huez, S. Perusin, S. Audion, TMS Annual Meeting Proceedings, Supplemental Proceedings, vol. 3, 2010, pp. 593–601.
[11] V. Sinha, J.E. Spowart, M.J. Mills, J.C. Williams, Metall. Mater. Trans. A 37 (2006) 1507–1518.
[12] V. Sinha, M.J. Mills, J.C. Williams, Metall. Mater. Trans. A 37 (2006) 2015–2026.
[13] F. Bridier, P. Villechaise, J. Mendez, Acta Mater. 56 (2008) 3951–3962.
[14] J.M. Gomez de Salazar, A. Urena, J.G. Carrion, Scr. Mater. 35 (1996) 479–484.
[15] V.V. Stolyarov, Met. Sci. Heat Treat. 49 (2007) 57–60.
[16] K. Prasad Rao, K. Angamuthu, P. Bala Srinivasan, J. Mater. Process. Technol. 199 (2008) 185–192.
[17] W. Zhou, K.G. Chew, Mater. Sci. Eng. A 347 (2003) 180–185.
[18] T. Mohandas, D. Banerjee, V.V. Kutumba Rao, Mater. Sci. Eng. A 254 (1998) 147–154.
[19] J.P. Hirth, F.H. Froes, Metall. Trans. A 8A (1977) 1749–1761.
[20] C. Buirette, J. Huez, N. Gey, E. Andrieu, G. Khelifati, J. Delfosse, Proceedings of the 2011 Titanium Conference, 2011.
[21] A.N. Stroh, Adv. Phys. 6 (1957) 418.
[22] A.L. Helbert, X. Feaugas, M. Clavel, Metall. Mater. Trans. A 27 (1996) 3043–3058.
[23] G. Lutjering, Mater. Sci. Eng. A 243 (1998) 32–45.
[24] C. Buirette, Ph.D., University of Toulouse, INPT, France, 2011.